#25-073
2025 AFS Proceedings ©American Foundry Society

Solidification of Medium Manganese Q&P Steels

Robert B. Tuttle
Western Michigan University, Kalamazoo, Michigan, USA

ABSTRACT

Quench and partition (Q & P) steels with medium manganese (Mn) content have attracted increasing interest for a variety of applications. This study examined two med-Mn steel alloys to better understand their solidification and phase reactions. Thermal analysis results were compared to thermodynamic predictions to determine the validity of the predictions. Overall, the thermodynamic predictions were fairly accurate in terms of the liquidus and peritectic temperatures. However, the solidus temperatures differed dramatically. The as-cast microstructure was fully martensitic, which was not expected. Computed Time-Temperature-Transformation (TTT) and Continuous Cooling Transformation (CCT) diagrams were done to determine the predicted structure, but these did not accurately predict the observed microstructure.

Keywords: solidification, thermal analysis, medium-Mn, steel

INTRODUCTION

Research into the third generation of advanced high strength steels (AHSS) has focused on medium levels (1-8 wt.%) of manganese. The interest in these alloys stems from their lower cost compared to 2nd generation AHSS steels.[1] The design of these alloys has depended on the strengthening mechanism: solid solution, transformation inducted plasticity (TRIP), twinning induced plasticity (TWIP), and multiphase.[2–8] Of these approaches, steels with TRIP or TWIP mechanisms combined with traditional phases provide the most promising combinations of strength and ductility. Steels processed through the quench and partition (Q&P) heat treatment are of particular interest.[1,9–15] This process involves austenitizing the steel followed by quenching at a set temperature (QT) which lies between the M_s and M_f temperature of the alloy. This causes the formation of austenite and martensite. Quenching is then followed by reheating the steel to a higher temperature for partitioning (PT). During partitioning, carbon from the martensite enters the austenite. This stabilizes the austenite at room temperature and encourages the TRIP mechanism.[7] The stabilized austenite forms additional martensite when the steel is plastically deformed increasing the alloy's strength and provides additional ductility.[7]

The design of Q&P steels centers on stabilizing austenite which can undergo the TRIP mechanism.[7,9,16] The C, Mn, and Al are employed as austenite stabilizers.[9] The use of high levels of Mn is necessary to minimize the amount of carbon while still stabilizing the austenite at room temperature. Silicon is frequently added to retard cementite formation to ensure austenite and martensite form within the microstructure.[9] The balance of martensite, ferrite, and retained austenite within the microstructure of the Q&P steel provides the ability to optimize the combination of strength and ductility of the alloy. Al can also assist in preventing cementite formation, but it can reduce the austenite fraction after partitioning. Thus, its use is limited but valuable.

Most proposed Q&P steel compositions reside between 0.1-0.5 wt.% C, 1-8 wt.% Mn, and 0.4-3 wt.% Si with other alloying elements. Prediction of solidification phase reactions, particularly the peritectic, have been difficult in these composition ranges.[17–21] The difficulty is related to several factors: a lack of sufficient thermodynamic data in the databases, significant segregation in some compositions that impede the use of differential scanning calorimetry (DSC), and the difficulty of identifying the peritectic in DSC experiments.[17,22]

The author has examined the use of a thermal analysis (TA) technique effectively employed in providing process control for cast iron and aluminum alloys for studying the solidification of steels.[23–26] The technique consists of pouring liquid steel directly from the melt into a small cup with a thermocouple. As the steel cools, the temperature is recorded and then analyzed. A typical sample mass in this technique is about 250g. The DSC samples are 100-200mg. The larger mass results in more overall energy from the various solidification reactions and enhances the ability to detect each peak on the cooling rate curve for a sample. While the most recent DSC systems may have the ability to detect the peritectic reaction, they still suffer sampling issues that this technique does not. Since TA employs a large sample directly from the melt, the samples are not affected by solidification segregation like the smaller samples for DSC. Thus, they can be more representative of the actual alloy.

The TA method has been employed by the author to examine steel solidification across multiple alloys.[24–34] In work by Tuttle and Kapdia, the addition of rare earth alloying elements were examined.[34] The goal was to determine why rare earth additions result in the grain

refinement of 4130. Rare earth additions resulted in no significant change in the liquidus, but a significant change in the peritectic temperature. This variation was associated with the formation of rare earth oxysulfide inclusions within the material and a refined structure. These authors also noted a disagreement between CALculation of PHAse Diagram (CALPHAD) predictions, reference data, and the measured peritectic temperature. All of the measured peritectic temperatures were higher than predicted. Work with HY100 found a similar, but smaller increase in the peritectic temperature when rare earth elements were added to the alloy.[33] Furthermore, CALPHAD predictions noted an increase in δ-ferrite stability in this alloy due to the presence of minute amounts of cerium.[33] No refinement was associated with the addition of rare earth. It appears the increase in δ-ferrite stability played a role.[33] Work on titanium master alloy additions saw no change in the peritectic temperature or other solidification reactions in 1030.[30] However, the author did find refinement of the microstructure. Titanium refinement appeared to be due to the formation of Ti(C,N) particles in the late stages or after solidification.[30] A Zener pinning refinement mechanism was proposed for the observed refinement in steels with titanium additions.[30] These varying areas of work demonstrate that the TA method provides a valuable tool for understanding steel solidification, even when reaction temperature changes are small.

To provide additional insight into the solidification of Fe-Mn-C-Si-Al alloys designed for the Q&P process, the author selected two alloy compositions: 0.20C-1.95Mn-1.7Si and 0.19C-2.5Mn-0.1Al-1.7Si. These alloys were selected based on their compositions being similar and lying within many of the proposed alloy compositions for Q&P steels. Prior experiments similar alloys show that these alloys have promising properties for automotive, aerospace, and industrial applications.[12,35] The purpose of this work was to compare CALPHAD solidification predictions to measurements of experimental heats employing the thermal analysis (TA) method. The parameters of interest were the liquidus, solidus, freezing range, and peritectic reaction temperature. Additionally, the test heats were cast into sand molds, so quantification of the as-cast microstructure and inclusion population were also conducted.

EXPERIMENTAL PROCEDURE

THERMODYNAMIC PREDICTIONS

Scheil solidification predictions were conducted using ThermoCalc© and the TCFE12 database. The actual alloy compositions were utilized for these computations. Carbon was assumed to be a fast diffuser.

MELTING AND THERMAL ANALYSIS PROCEDURE

A 23 kg heat of each alloy was melted in a 3 kHz induction furnace under normal atmosphere. The furnace was lined with alumina refractory. The initial charge consisted of 1010 punchings. Once the melt achieved 1650C (3002F), graphite, FeSi, electrolytic Mn, and, if necessary, Al shot was added. Heating continued until 1730C (3146F) when a 2.3 kg sample of the melt was extracted. This sample was then poured into a TA cup (Figure 1) that contained a Type S thermocouple. A MeltLab system was used to record temperature data at a rate of 38.4 kHz. Existing data smoothing, derivative calculation, and liquidus and solidus algorithms within the system were utilized.

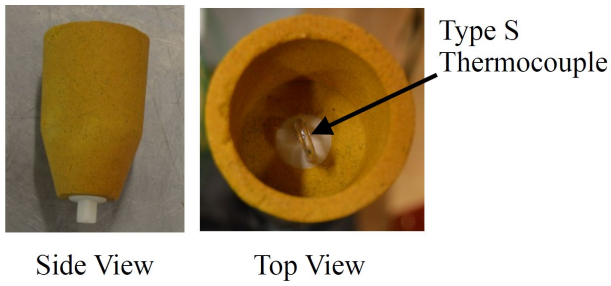

Figure 1. Typical TA cup employed in this work.

The remainder of the melt was poured into a mold to make 25mm thick Y-block castings (Figure 2). The molds were made using a silica sand with an AFS GFN of 55 and a 2 wt.% phenolic urethane nobake binder. Molds were manually compacted. The pouring temperature was 1590C (2894F). Molds were shaken out after 30 minutes and then allowed to continue air cooling.

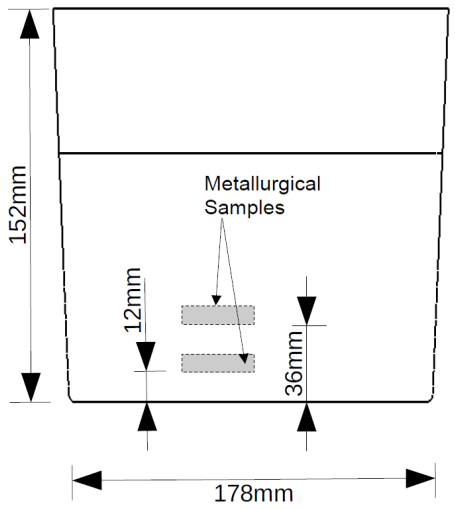

Figure 2. Schematic of Y-block casting and metallurgical sample location.

After cooling to room temperature, the Y-block was sectioned to remove two specimens from each casting. One is located approximately 12 mm from the bottom, and one located 36 mm. Both were near the center of the casting (Figure 2). These were further sectioned by a diamond precision saw and mounted into conductive mounts. The samples were ground with SiC papers in the following grit order: 320, 400, 600, 800, and 1200. Polishing consisted of a 1 µm polycrystalline diamond followed by a 0.05 µm alumina. Samples were etched with 3% Nital to reveal the microstructure.

A portion of the material from the 12 mm location was also utilized for determining the final alloy composition. After sectioning, a 60 grit zirconia sanding belt prepared the surface. A Hitachi Foundrymaster optical emission spectrometer (OES) analyzed the alloy composition. Analysis of the as-cast microstructure and inclusions were conducted on a JEOL JSM-IT200 scanning electron microscope (SEM) with an energy dispersive spectrometer (EDS). An accelerating voltage of 20kV and working distance of 10 mm were employed. For quantitative analysis of inclusions, the compositions were assumed to be oxides.

RESULTS AND DISCUSSION

THERMODYNAMIC ANALYSIS

Table 1 lists the actual compositions of each heat. Several elements were higher than expected but still appeared to be similar enough to the target alloys. There was some difficulty in analyzing the QP1 heat since the Mn content required the use of a general steel calibration on the spectrometer. This general calibration results in more uncertainty in the composition (~ +/- 0.5 wt.%). The selected compositions were at the edge of the med-Mn specific calibration program, so this difficulty was not surprising.

Table 1. Alloy Compositions for each Heat

Alloy	C [wt.%]	Mn [wt.%]	Si [wt.%]	Al [wt.%]
QP1	0.25	3.38	1.70	0.03
QP2	0.27	2.20	1.90	-

Figure 3 depicts the Scheil calculation results for the QP1 alloy. The phase reaction temperatures are listed in Table 2. Based on the predictions, 30% of the solidification range occurs with only δ-ferrite and liquid. For this alloy, the peritectic reaction results in complete transformation to austenite and no δ-ferrite + austenite phase region was predicted. The freezing range was estimated to be 146°C (263°F). This is a relatively large freezing range which can result in dispersed porosity issues in the alloy. Figure 4 depicts the same results for the QP2 alloy. Table 2 lists the phase reaction temperatures in that alloy as well. This alloy appears to spend 50% of its solidification range in the δ-ferrite phase field. It is also not predicted to have a δ-ferrite + austenite phase region. QP2 was predicted to have a large freezing range of ~144°C (260°F) according to the thermodynamic calculations.

Table 2. Phase Reaction Temperature Predictions

Alloy	Liquidus [°C]	Peritectic [°C]	Solidus [°C]
QP1	1477	1460	1331
QP2	1479	1453	1335

Close examination of Table 2 shows that the liquidus, solidus, and peritectic temperatures are within 3–7°C for the two alloys. QP2 has slightly lower liquidus and solidus temperatures, but a slightly shorter freezing range.

The long freezing range of both alloys does indicate some possible difficulties with the alloys. Long freezing range alloys tend to have more problems with dispersed porosity and hot tearing.[36–40] The larger freezing range results in longer dendrites at the same cooling rate when compared to other alloys. This leads to dendrite impingement limiting liquid metal flow to the entire solidification front which reduces feeding while the metal is solidifying. The implication is that these alloys will require more feeding/risering to reduce porosity and may be more prone to hot tearing than shorter freezing range alloys. An example of a shorter freezing range low alloy steel would be 4130, which has a freezing range of 40°C (72°F).

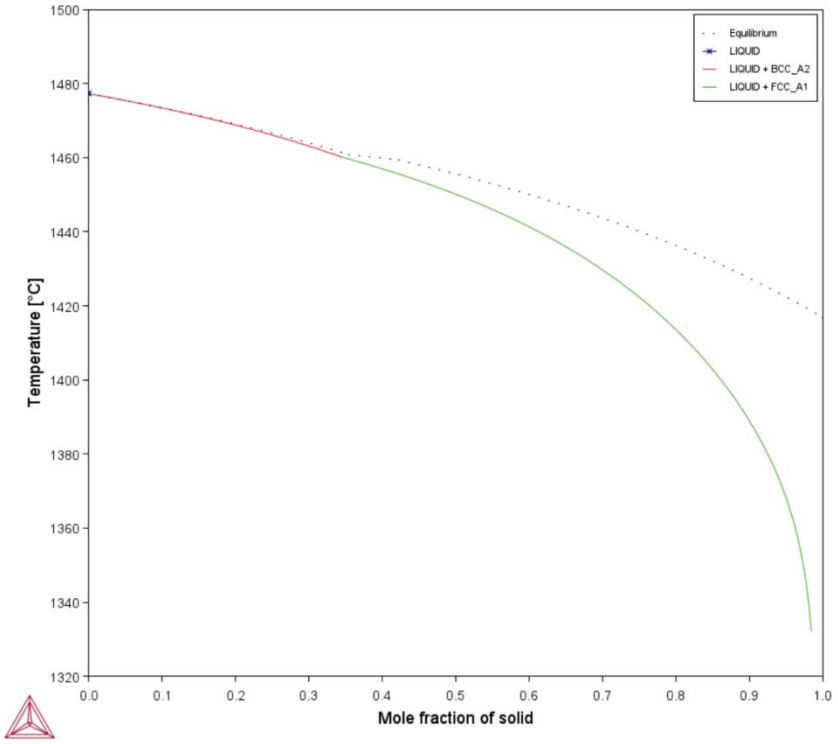

Figure 3. Scheil prediction of QP1 alloy.

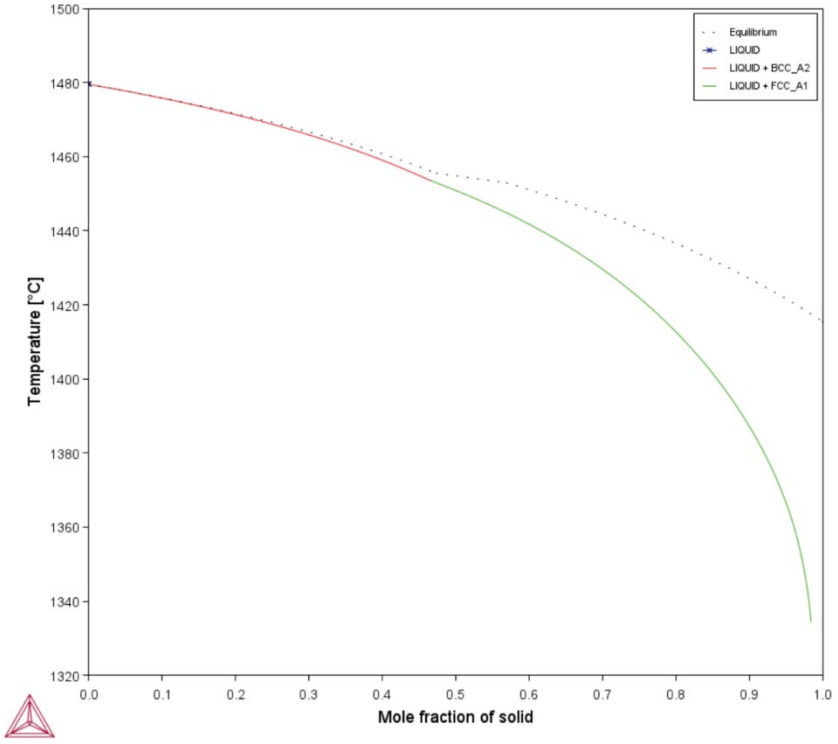

Figure 4. Scheil prediction for QP2 alloy.

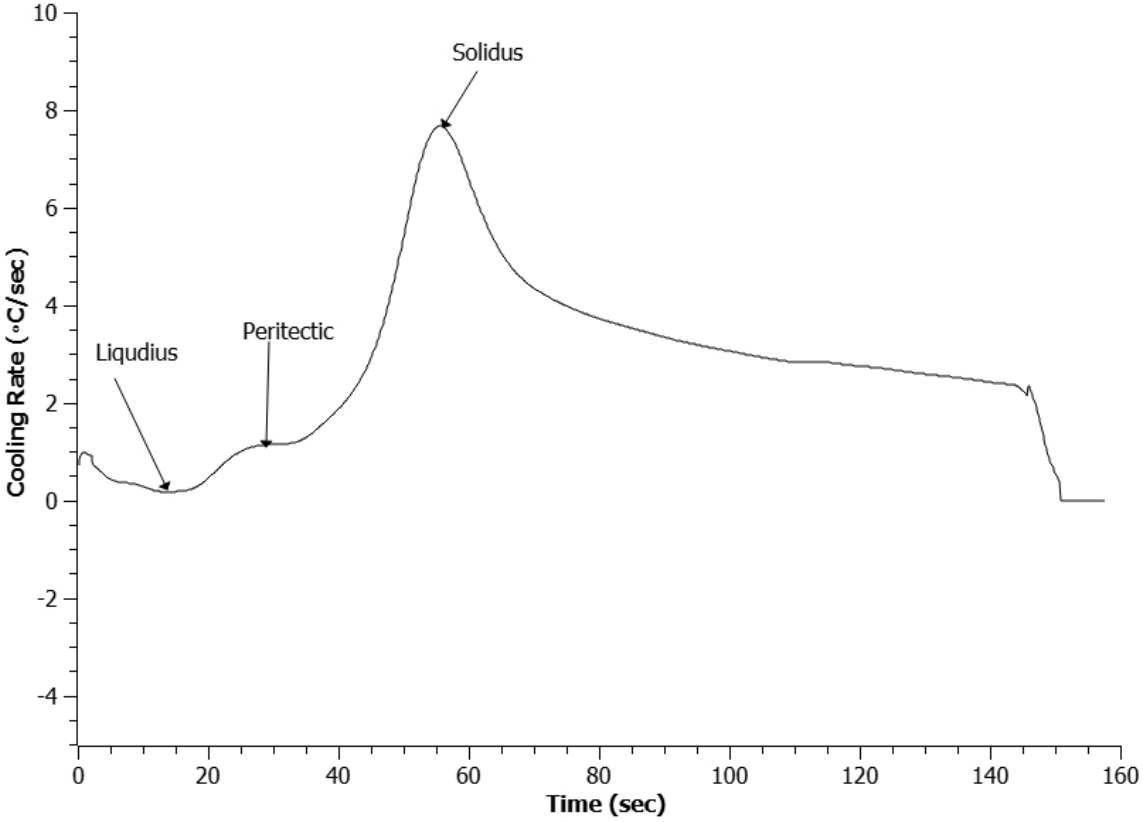

Figure 5. Cooling curve with phase reactions labeled for QP1 alloy.

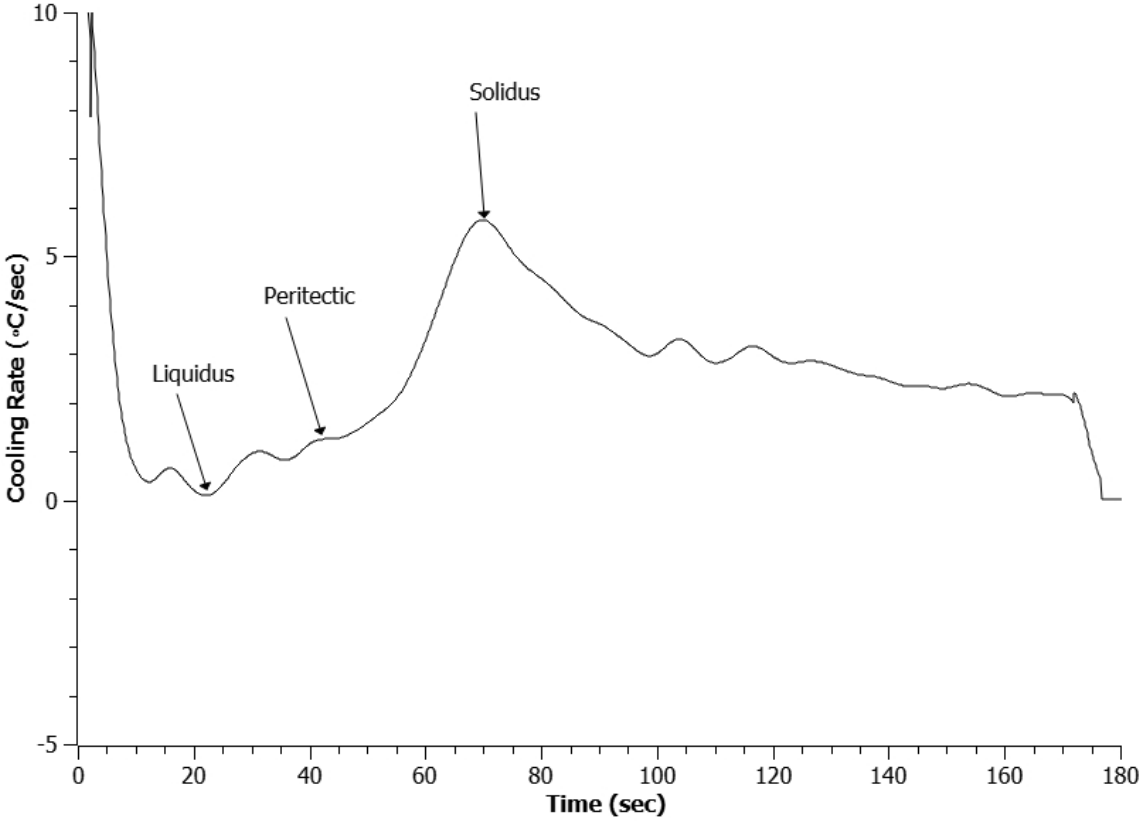

Figure 6. Phase reactions and cooling curve for QP2 alloy.

THERMAL ANALYSIS RESULTS

Figures 5 and 6 present the measured cooling curves for each alloy. The liquidus, peritectic, and solidus are labeled in each figure. The liquidus was determined as the point on the curve with a cooling rate near zero while the solidus was the largest peak. As stated before, these measurements were made using the existing algorithms in the TA software. Peritectic identification was done manually by identifying the first peak to the left of the solidus peak. Interestingly, the QP2 alloy had an additional peak between the liquidus and peritectic. It was not apparent what this peak was associated with.

Table 3. Measured Solidification Reaction Temperatures

Alloy	Liquidus [°C]	Peritectic [°C]	Solidus [°C]	Freezing Range [°C]
QP1	1473	1463	1379	94
QP2	1473	1455	1374	99

Table 3 lists the measured solidification reaction temperatures. It was found that the liquidus temperatures were similar for both alloys and close to the thermodynamic predictions. However, the solidus temperatures were higher by approximately 40°C (72°F). Unlike the thermodynamic predictions, the QP2 alloy had the largest freezing range. However, the freezing range was much shorter (~ 45°C/81°F) than predicted for either alloy. The peritectic temperatures were close between the measured and predicted values.

There are multiple factors which might contribute to the differences between the thermodynamic solidus predictions and the measured values. First, the databases for alloy compositions in this range have not yet had sufficient data in them to reliably predict phase reactions.[17,26,41] Another factor is that much of the data within the databases employed by calculation of phase diagram (CALPHAD) software tend to use differential scanning calorimetry (DSC) experimental data.[42] DSC employs samples typically in the 100-200 mg size range for solidification studies.[22] These are relatively large sample sizes for DSC since the solidification reactions evolve smaller energy quantities compared to many solid state reactions.[22] Thus correctly identifying them is difficult with this experimental technique. While some researchers have attempted to find analysis or experimental techniques that address these issues, it is not yet clear these fully address all issues.[17,19,26,43] How this relates to CALPHAD software is that since DSC data has been preferentially used in the databases it can result in inaccurate data for the predictions to be based upon. The author's technique provides an additional set of data where phase evolution is much easier to determine due to sample size.[26] A final factor that could impact the difference between the thermodynamic predictions and measured values is the cooling rate of the steel. Carlsson and Callmer found broad evidence of a strong dependency between cooling rate and solidification reaction temperatures in steels.[44] This dependency occurred for all phase reaction temperatures.[44] If the data employed for the thermodynamic predictions has a different cooling rate than the samples in this study then a significant difference would be expected. Unfortunately, it is not easy to determine the cooling rate the database data was acquired with. However, the strong agreement for the liquidus and solidus provide some sense that the predictions are relatively accurate. A final factor is that the Scheil calculations may be over predicting the segregation that occurs in the alloys. High segregation would result in a much lower liquidus temperature for the remaining liquid. Thus, a lower solidus would be predicted. If this does not occur in the real alloys, then the solidus would be higher as observed in this work. It remains difficult to determine which factor is playing the main role in the discrepancies. Nevertheless, it is apparent that the solidus temperatures are higher than thermodynamic predictions are indicating.

MICROSTRUCTURE AND INCLUSION CHARACTERIZATION

The as-cast microstructure of both alloys was examined in a SEM with EDS. A martensitic structure was observed in both alloys (Figures 7 and 8). This was unexpected since a ferritic structure with carbides in either pearlite or another phase had been anticipated. It appears that, despite cooling within the mold for 30 minutes prior to shakeout, the casting had been hot enough that the cooling rate in air allowed the formation of martensite. The martensite appeared slightly coarser in the QP2 steel.

Figure 7. Typical microstructure of as-cast QP1.

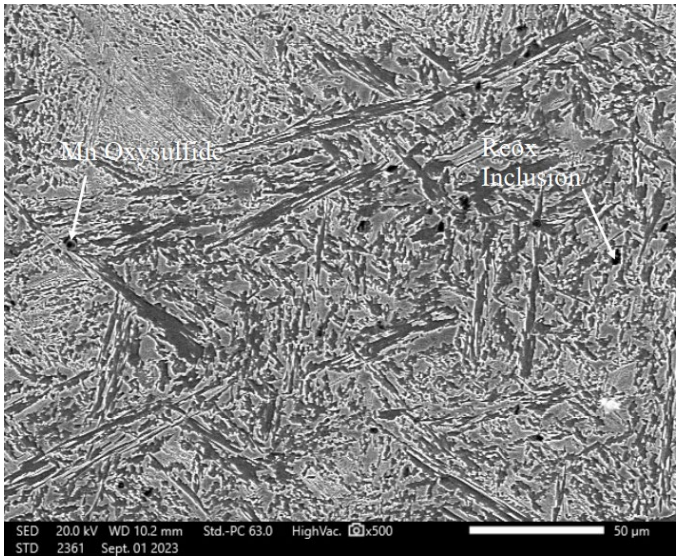

Figure 8. Typical microstructure and inclusions from QP2 alloy.

Analysis of the inclusions in both steels revealed MnS and some oxysulfides. The formation of large MnS has been broadly reported in med-Mn steels.[45–47] The reoxidation inclusion in Figure 7 had a composition of: 23.3 wt.% Fe, 2.49 wt.% Mn, 3.83 wt.% Ca, 37.79 wt.% Al, and 31.05 wt.% O. The Mn oxysulfide in Figure 8 had a composition of: 3.58 wt.% Fe, 42.2 wt.% Mn, 22.12 wt.% S, 1.87 wt.% Si, 7.24 wt.% Al, and 18.9 wt.% O. The reoxidation inclusion in Figure 8 had a composition of 50.23 wt.% Fe, 9.64 wt.% Mn, 1.90 wt.% S, 10.79 wt.% Si, 5.36 wt.% Al, and 21.37 wt.% O. These inclusions were typical for both alloys, and there appeared to be little difference.

To examine the cause more closely for the as-cast martensitic microstructure, the casting simulation results were reexamined and a TTT diagram was calculated in ThermoCalc© using the TCFE12 database and an average grain size of 100 µm for each alloy. Figure 9 presents the simulated cooling rate for the Y-block casting. The cooling rate is around 0.7°C (1.26°F)/s across the regions where the samples were extracted (See Figure 9). Additionally, the solidification simulation indicated the steel should have been around 630C (1166F) when shakeout occurred. This was well below the A_1 temperature of the alloy. Figure 10 provides the TTT diagram for the QP2 alloy. QP1 was very similar, but with reaction times at longer times, so it is not presented for brevity. Based on the cooling rate from the solidification simulation, there should have been significant amounts of ferrite to form even if some austenite remained at shakeout. Based on microstructural observations, it would appear that the computed TTT diagram does not represent actual behavior in this system.

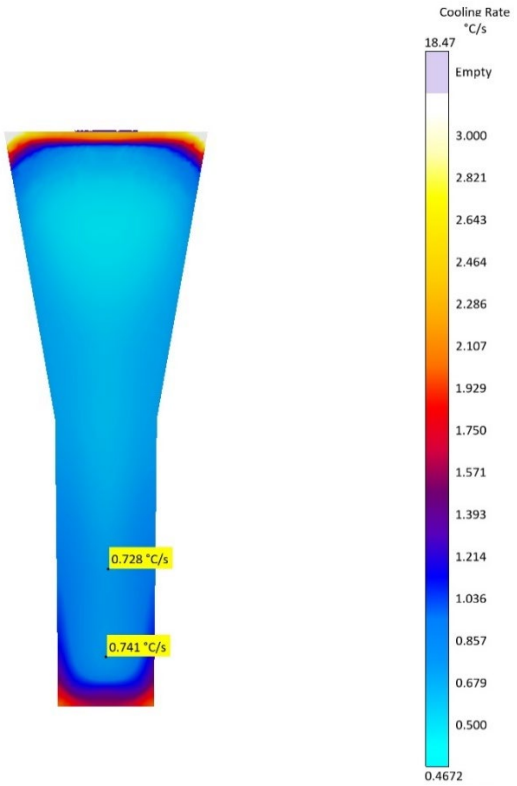

Figure 9. Cooling rate for the Y-block casting.

The author attempted to compute CCT diagrams for both alloys; however, these did not appear correct since they lacked prediction for several phase reactions (Figure 11). ThermoCalc© was only able to determine the ferrite start, austenite 50%, austenite 98%, and martensite start reaction lines for QP1. While the limitations of Figure 11 are obvious, the diagram does provide support for the author's original theory that the steel should have contained significant amounts of ferrite in the as-cast structure.

The 1 K/s cooling rate line in Figure 11, which is green, indicates that ferrite with some martensite might form. Considering the cooling rate in the casting had been around 0.7 K/s and the time to shakeout had been 30 minutes (1,800 sec), small fractions of martensite might have been formed according to Figure 11. Based on the as-cast structure of both steels, it is apparent that martensite forms easily in these alloys. Computed TTT and CCT diagrams did not predict this occurrence. It seems that the diffusion and meta-phase reaction data are not complete for these alloys.

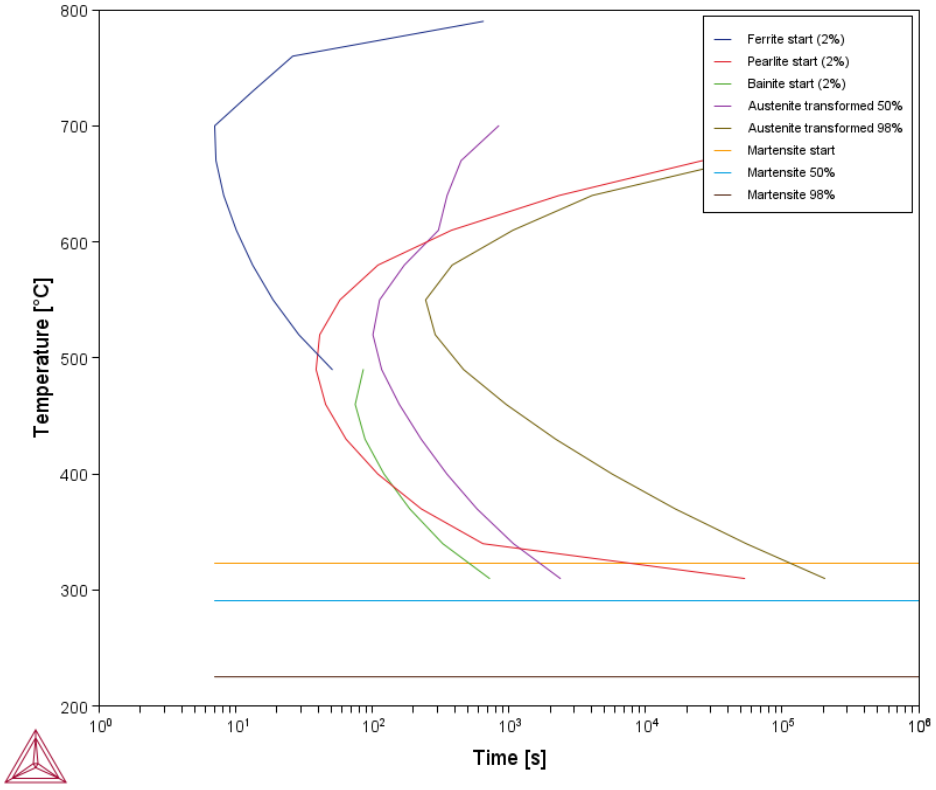

Figure 10. Computed TTT diagram for QP2.

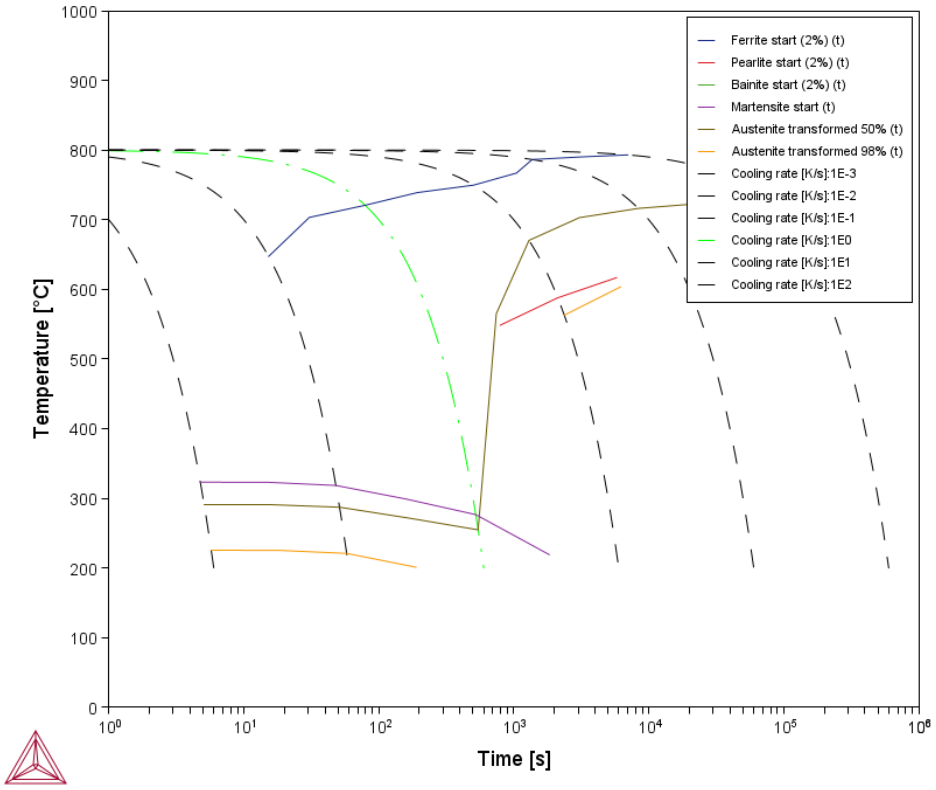

Figure 11. Computed CCT diagram for QP2.

CONCLUSION

Two similar med-Mn, Q&P style steels were analyzed for their solidification and as-cast microstructure. The thermal analysis technique employed easily identified the various solidification reactions. This was likely due to the larger sample size employed in this technique. Thermal analysis data found that the liquidus and peritectic reactions occurred at temperatures very similar to the thermodynamic predictions. The solidus temperatures were much higher (~40°C) which also meant the freezing ranges were shorter.

The as-cast microstructure was martensite, which was not expected. Thermodynamic predictions of the TTT and CCT diagrams of the alloys had indicated that the steels should have had a ferritic microstructure in the as-cast state. This discrepancy indicates that the steels were much more hardenable than expected. Furthermore, it indicates that the TTT and CCT data for these alloys are insufficient for accurate predictions.

ACKNOWLEDGEMENTS

The author would like to acknowledge the help of Mujeeb Shiak and Jacob Paquette in pouring the experimental heats. He would also like to thank Jennie Tuttle for her editorial assistance.

REFERENCES

1. Lesch, C., Kwiaton, N. & Klose, F.B., "Advanced High Strength Steels (AHSS) for Automotive Applications − Tailored Properties by Smart Microstructural Adjustments," *Steel Research International*, vol. 88 (10), pp. 1700210 (2017).
2. Qu, H., Michal, G.M. & Heuer, A.H., "Third Generation 0.3C-4.0Mn Advanced High Strength Steels Through a Dual Stabilization Heat Treatment: Austenite Stabilization Through Paraequilibrium Carbon Partitioning," *Metallurgical and Materials Transactions A*, vol. 45 (6), pp. 2741–2749 (2014).
3. Glage, A., Weidner, A. & Biermann, H., "Cyclic Deformation Behaviour of Three Austenitic Cast CrMnNi TRIP/TWIP Steels with Various Ni Content," *Steel Research International*, vol. 82 (9), pp. 1040–1047 (2011).
4. Jahn, A., Steinhoff, K.-P., et al., "Phosphor Alloyed Cr-Mn-Ni Austenitic As-cast Stainless Steel with TRIP/TWIP Effect," *Steel Research International*, vol. 85, pp. 477–485 (2014).
5. Wang, H., Kang, J., et al., "Microstructure and mechanical properties of hot-rolled and heat-treated TRIP steel with direct quenching process," *Materials Science and Engineering: A*, vol. 702, pp. 350–359 (2017).
6. Mohapatra, J. N., Dabbiru, S. K. & Balachandran, G., "Development of Ultra-high Strength Steel with a Versatile Range of Properties by Single Stage Quench Partitioning Process," *Transactions of the Indian Institute of Metals*, vol. 76 (7), pp. 1905–1913 (2023).
7. Speer, J.G., Streicher, A.M., Matlock, D.K., Rizzo, F. & Krauss, G., "Quenching and Partitioning: A Fundamentally New Process to Create High Strength TRIP Sheet Microstructures," *Austenite Formation and Decomposition*, pp. 505–522 (2003).
8. Moor, E.D., Speer, J.G., Matlock, D.K., Kwak, J.-H. & Lee, S.-B., "Effect of Carbon and Manganese on the Quenching and Partitioning Response of CMnSi Steels," *ISIJ International*, vol. 51 (1), pp. 137–144 (2011).
9. Kumar, S. & Singh, S.B., "Quenching and Partitioning (Q&P) Steel: Alloy Design, Phase Transformation and Evolution of Microstructure," *Metallurgical and Materials Transactions A*, vol. 54 (8), pp. 3134–3156 (2023).
10. Tian, Y., Tan, Z., Wang, J. & Zhang, M., "Realization of quenching & dynamic partitioning on large-size parts," *Materials and Manufacturing Processes*, vol. 37 (13), pp. 1490–1499 (2022).
11. Del Molino, E., Arribas Telleria, M., et al., "Influence of Ni and Process Parameters in Medium Mn Steels Heat Treated by High Partitioning Temperature Q&P Cycles," *Metallurgical and Materials Transactions A*, vol. 53 (11), pp. 3937–3955 (2022).
12. Cao, R., Liang, J., Li, F., Li, C. & Zhao, Z., "Intercritical Annealing Processing and a New Type of Quenching and Partitioning Processing, Actualized by Combining Intercritical Quenching and Tempering, for Medium Manganese Lightweight Steel," *Steel Research International*, vol. 91 (1), pp. 1900335 (2020).
13. Zhang, K., Liu, P., Li, W., Ma, F., Guo, Z. & Rong, Y., "Enhancement of the Strenght and Ductility of Martensitic Steels by Carbon," *Materials Science and Engineering: A*, vol. 716, pp. 87–91 (2018).
14. Wendler, M., Ullrich, C., et al., "Quenching and Partitioning (Q&P) Processing of Fully Austenitic Stainless Steels," *Acta Materialia*, vol. 133, pp. 346–355 (2017).
15. Speer, J. G., De Moor, E. & Clarke, A. J., "Critical Assessment 7: Quenching and partitioning," *Materials Science and Technology*, vol. 31 (1), pp. 3–9 (2015).
16. Wang, L. & Speer, J. G., "Quenching and Partitioning Steel Heat Treatment," *Metallography, Microstructure, and Analysis*, vol. 2 (4), pp. 268–281 (2013).

17. Abraham, S., Bodnar, R., Lonnqvist, J., Shahbazian, F., Lagerstedt, A. & Andersson, M., "Investigation of Peritectic Behavior of Steel Using a Thermal Analysis Technique," *Metallurgical and Materials Transactions A*, vol. 50 (5), pp. 2259–2271 (2019).
18. Azizi, G., Thomas, B.G. & Asle Zaeem, M., "Review of Peritectic Solidification Mechanisms and Effects in Steel Casting," *Metallurgical and Materials Transactions B*, vol. 51 (5), pp. 1875–1903 (2020).
19. Bernhard, M., Presoly, P., Bernhard, C., Hahn, S. & Ilie, S., "An Assessment of Analytical Liquidus Equations for Fe-C-Si-Mn-Al-P-Alloyed Steels Using DSC/DTA Techniques," *Metallurgical and Materials Transactions B*, vol. 52 (5), pp. 2821–2830 (2021).
20. Zhuang, C., Liu, J., Li, C. & Tang, D., "Study on high temperature solidification behavior and crack sensitivity of Fe-Mn-C-Al TWIP steel," *Scientific Reports*, vol. 9 (1), pp. 15962 (2019).
21. Balogun, D., Roman, M., Gerald, R.E., Bartlett, L., Huang, J. & O'Malley, R., "A Study on the Impact of Silicon and Manganese on Peritectic Behavior in Low Alloy Steels Assisted by Mold Thermal Mapping Technology and Shell Growth Measurements," *Metallurgical and Materials Transactions B*, vol. 54 (3), pp. 1326–1341 (2023).
22. Boettinger, W.J., Kattner, U.R., Moon, K. & Perepezko, J., "NIST Recommended Practice Guide: DTA and Heat-flux DSC Measurements of Alloy Melting and Freezing," vol. Special Publication 960-15 NIST, Gaithersburg, MD, (2006).
23. Stefanescu, D.M., "Thermal Analysis—Theory and Applications in Metalcasting," *International Journal of Metalcasting*, vol. 9 (1), pp. 7–22 (2015).
24. Kapadia, H.A., Tuttle, R.B., "A System for the Thermal Analysis of Steels," *Modern Casting*, vol. 110 (3), pp. 33-41 (2020).
25. Tuttle, R., "Thermal Analysis Experiments in Titanium and Magnesium Additions to 4130 Steel," *Journal of Materials Engineering and Performance*, vol. 29 (9), pp. 5913–5922 (2020).
26. Tuttle, R.B., "Peritectic Determination by a Melt Deck Thermal Analysis System," *Archives of Foundry Engineering*, vol. 19 (1), pp. 83–88 (2019).
27. Tuttle, R., "Effect of Ti Master Alloys in HY100," *Transactions of the American Foundry Society*, vol. 130, pp. 381-390 (2022).
28. Tuttle, R., "Effect of Rare Earth Master Alloys on 4130," *International Journal of Metalcasting* (2021).
29. Tuttle, R., "Comparison of Rare Earth Refinement in 4130 and HY100," *Metals*, vol. 11 (4), pp. 540 (2021).
30. Tuttle, R., "Titanium Master Alloy Effect on 1030," *Transactions of the American Foundry Society*, vol. 129, pp. 357–367 (2021).
31. Tuttle, R., "Effect of RE Master Alloys on AISI 1030," *Proceedings of AISTech 2021*, pp. 406–419 (2021).
32. Tuttle, R.B., "Effect of Magnesium and Titanium on the Mechanical Properties of HY100," *Proceedings of AISTech 2020* (2020).
33. Tuttle, R.B., "Thermal Analysis of Rare Earth Additions to HY100," *Journal of Materials Engineering and Performance*, vol. 28 (5), pp. 2707–2715 (2019).
34. Tuttle, R. & Kapadia, H.A., "Thermal Analysis of Rare Earth Grain Refined 4130," *International Journal of Metalcasting*, vol. 13 (2), pp. 273–285 (2018).
35. Cheng, Y.Y., Zhao, G., Xu, D. M., Mao, X.P., Bao, S.Q. & Yang, G.W., "Comparative Study on Microstructures and Mechanicla Properties of Q&P Steels Prepared with Hot-rolled and Cold-rolled C–Si–Mn Sheets," *Journal of Materials Research and Technology*, vol. 20, pp. 1226–1242 (2022).
36. Stefanescu, D., "Science and Engineering of Casting Solidification," Springer, New York, NY, (2015).
37. Tuttle, R.B., "Foundry Engineering: The Metallurgy and Design of Castings," CreateSpace Independent Publishing Platform, Charleston, SC, (2012).
38. Lu, Y., Bartlett, L.N. & O'Malley, R.J., "A Review on Hot Tearing of Steels," *International Journal of Metalcasting*, vol. 16 (1), pp. 45–61 (2022).
39. Davidson, C., Viano, D., Lu, L. & St. John, D., "Observation of Crack Initiation during Hot Tearing," *International Journal of Cast Metals Research*, vol. 19 (1), pp. 59–65 (2006).
40. Eskin, D. G., Suyitno & Katgerman, L., "Mechanical properties in the semi-solid state and hot tearing of aluminium alloys," *Progress in Materials Science*, vol. 49 (5), pp. 629–711 (2004).
41. Wang, W., An, Z., Luo, S. & Zhu, M., "In-situ observation of peritectic solidification of Fe-Mn-Al-C steel with medium manganese," *Journal of Alloys and Compounds*, vol. 909, pp. 164750 (2022).
42. Lukas, H.L., Fries, S.G. & Sundman, B., "Computational Thermodynamics: The CALPHAD Method," Cambridge University Press, Cambridge ; New York, (2007).
43. Binczyk, F., Cwajna, J. & Gradoń, P., "ATD and DSC Analysis of IN-713C and ZhS6U-VI Superalloys," *Archives of Foundry Engineering*, vol. 17 (1), pp. 13–16 (2017).
44. Carlsson, B. & Callmer, B., "A Guide to the Solidification of Steels," Jenkortoret, Stockholm, (1977).
45. Wang, G.-T., Zhou, Y.-L., Wang, L.-J. & Liu, C.-M., "Study on Microstructures and Properties of Low-Carbon-Steel Heavy Plate Treated by Quenching and Dynamic Partitioning," *Journal of Materials Engineering and Performance*, vol. 31 (2), pp. 1195–1203 (2022).
46. Mohammadi Zahrani, M., Ketabchi, M. & Ranjbarnodeh, E., "Microstructure Development and Mecanical Properties of a C-Mn-Si-Al-Cr Cold Rolled Steel Subjected to Quenching and Partitioning

Treatment," *Journal of Materials Research and Technology*, vol. 22, pp. 2806–2818 (2023).

47. HajyAkbary, F., Sietsma, J., Petrov, R.H., Miyamoto, G., Furuhara, T. & Santofimia, M. J., "A Quantitative Investigation of the Effect of Mn Segregation on Microstructural Properties of Quenching and Partitioning Steels," *Scripta Materialia*, vol. 137, pp. 27–30 (2017).